

Mar.2014 / Vol.145

M i t s u b i s h i E l e c t r i c

ADVANCE

Advanced Technologies of Automobile Devices for Smart Society

• **Editorial-Chief**

Kiyoshi Sakai

• **Editorial Advisors**

*Toshio Masujima
Mitsutaka Matsukura
Makoto Egashira
Chikao Nishida
Hideaki Okada
Yoshiki Hama
Tetsuyuki Yanase
Takefumi Tsukada
Tatsuya Ichihashi
Masato Nagasawa
Daisuke Kawai
Masato Oshita
Toshihiro Kurita*

• **Vol. 145 Feature Articles Editor**

Yoichi Kadota

• **Editorial Inquiries**

Kiyoshi Sakai
Corporate Total Productivity Management
& Environmental Programs
Fax +81-3-3218-2465

• **Product Inquiries**

Masato Oshita
Automotive Equipment
Fax: +81-3-3218-2931

Mitsubishi Electric Advance is published on line quarterly (in March, June, September, and December) by Mitsubishi Electric Corporation. Copyright © 2014 by Mitsubishi Electric Corporation; all rights reserved. Printed in Japan.

The company names and product names described herein are the trademarks or registered trademarks of the respective companies.

CONTENTS

Technical Reports

Overview1
by *Yutaka Ohashi*

Eco-Driving Assistance with In-vehicle Information System2
by *Yuko Ohta* and *Hisashi Sugawara*

LED Headlamp Driver5
by *Yasuhiro Nukisato* and *Naohiro Kishi*

High Efficiency Isolated AC/DC Converter with Gradationally Controlled Voltage Inverter for On-board Charger8
by *Takashi Kaneyama* and *Ryota Kondo*

Next-generation Motor Controller Unit for Electric Power Steering11
by *Yoshihito Asao* and *Yoshihiko Kimpara*

Study of Fuel Adhesion Behavior during Spray-wall Impingement in PFI Engine13
by *Takashi Yonezawa* and *Kazuhiko Kawajiri*

Telematics-compatible Information Security Technology16
by *Nobuhiro Kobayashi* and *Manabu Misawa*

Precis

Along with the motorization of societies worldwide, there is growing demand for environmental, energy and safety solutions as well as for greater convenience and comfort.

As automobile functions become increasingly electronic, Mitsubishi Electric will continue to integrate its proprietary electronic, electric and control technologies to deliver such functions promptly, thus contributing to the automobile society of the future.

Overview



Author: *Yutaka Ohashi**

In order for automobiles to continue to be a safe and comfortable means of transportation, it is essential to eliminate those factors that hinder the creation of a low-carbon, safe and secure society. Automobile users want to be able to use various information services while driving, while elderly drivers want features that make driving safer. To meet such needs, automobile devices need to be improved and new functions developed. Environmentally, there is a shift from engines to motor drives such as those in hybrid electric vehicles, which require high efficiency motors and inverters. It is also important to reduce the fuel cost of conventional engine vehicles, such as by developing idling stop systems and other technologies for improving fuel efficiency. Meanwhile, active safety systems that use radar and cameras to monitor the surroundings of the vehicle are needed to improve safety. For greater convenience and comfort amid the growth of information and communications services, security technologies are indispensable for protecting the in-vehicle electronic system from malicious access and other threats. Mitsubishi Electric will continue to integrate its advanced technologies to develop such automobile devices, thus helping to create a smart, safe society with low-carbon emissions and a better life.

Eco-Driving Assistance with In-vehicle Information System

Authors: *Yuko Ohta** and *Hisashi Sugawara***

1. Introduction

This paper proposes an eco-driving pattern that takes traveling time into consideration. We performed a computer traffic simulation and field tests to evaluate the effects of eco-driving on fuel economy and surrounding traffic. As a result, the proposed driving pattern was confirmed to reduce the fuel consumption of both the eco-driving assisted vehicle and all traffic without adversely affecting the surroundings.

2. Eco-driving with In-vehicle Information System

This section describes the eco-driving assistance with the in-vehicle information system, which consists of: (1) a car navigation system, which provides a driving route map and infrastructure information, (2) a recommended-speed determination system, which calculates an eco-driving pattern based on the provided information such that the pattern is optimized for the road profile, signal schedule and other conditions en route, and (3) a display equipment, which informs the driver of the recommended speed.

The eco-driving pattern depends on the surrounding traffic, signal schedule, etc. Therefore, if the traveling time deviates from the expected driving schedule, it will be difficult to drive the vehicle as expected or the surrounding traffic may be adversely affected. Therefore, the eco-driving should be designed taking into consideration not only optimized energy consumption but also the traveling time. In the proposed system for generating the eco-driving pattern, adverse effects on the surrounding traffic are reduced by minimizing the delay from the estimated passing time en route. Figure 1 shows a sample pattern of the proposed eco-driving, where energy consumption during driving is reduced by controlling the acceleration when approaching an intersection with traffic signals. It is known that the acceleration pattern significantly affects fuel economy, and thus by reducing the acceleration rate, the fuel economy is expected to be improved. In this example, when approaching the first signal, keeping a constant speed prevented wasted acceleration before the red light. At the second signal, the amount of acceleration and deceleration was reduced before and after the intersection by estimating the timing of signal change and controlling the speed to an appropriate level for passing

through the intersection.

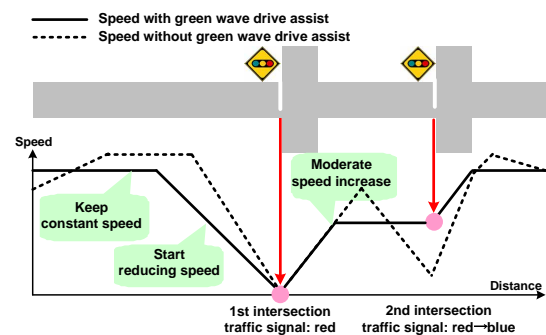


Fig. 1 Example of eco-driving with in-vehicle information system

3. Evaluation by Computer Simulation

We first performed a computer traffic simulation to evaluate the advantages of the proposed eco-driving and any adverse influence on the surrounding traffic. Figure 2 illustrates the road network used in this simulation, which contains nine intersections with traffic signals and vehicles joined at two of them. The road has one lane in each direction, the speed limit is set to 50 km/h, the signal cycle time is fixed to 100 seconds with the green split of 50%, and the offset is set to either 0 or 50 seconds depending on the distance between the intersections.

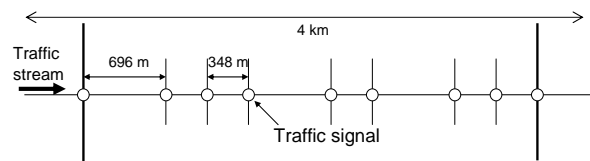


Fig. 2 Road network used in traffic simulation

Both quiet and busy traffic conditions were simulated at various traffic flow rates ranging from 60 to 840 vehicles/h. It was also assumed that eco-driving assisted and normal-driving vehicles were running together, which was then simulated by changing the ratios of eco-driving assisted vehicles from 0 to 100%.

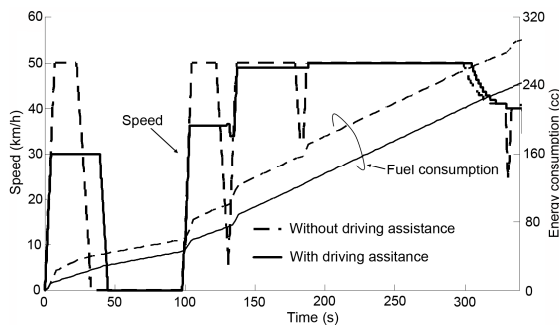
In the simulation, each normal-driving vehicle runs at a target speed determined by the road speed limit and the driver's personality, and decelerates or stops according to the distance from the vehicle in front and the current status of signals. In contrast, each eco-driving assisted vehicle runs at a speed limited by the recommended speed given by the proposed eco-driving pattern,

but otherwise accelerates or decelerates in the same manner as the normal-driving vehicle.

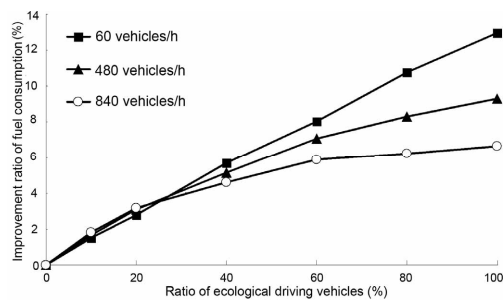
Figure 3 (a) shows an example where the vehicles assisted by the eco-driving system account for 80% of the total traffic flow of 720 vehicles/h. The driving speed and the fuel consumption data are shown for a certain vehicle driving under the same condition with and without the eco-driving assistance. In this example, regardless of the driving assistance, the traveling time was the same and the eco-driving did not cause any delay in the arrival time. In addition, the eco-driving led to early release of the accelerator pedal, thus reducing both the driving speed and the number of stops at traffic signals, and reducing fuel consumption by about 18%.

To evaluate the impact of the eco-driving on the overall traffic, Fig. 3 (b) shows the percentage of improvement in fuel economy compared to traffic with normal-driving vehicles only.

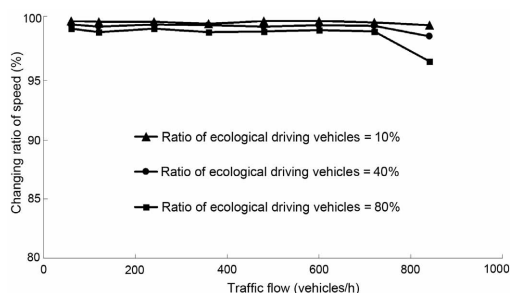
The chart indicates that the higher the percentage of eco-driving assisted vehicles, the lower the fuel consumption of the overall traffic; and the lower the traffic flow rate, the greater the improvement in fuel economy. In this evaluation, a maximum reduction in fuel consumption of 13% was obtained.



(a) Driving pattern of eco-driving assisted vehicle



(b) Improvement in total fuel consumption of all vehicles



(c) Change in average speed due to eco-driving assisted vehicles

Fig. 3 Results of traffic simulation

Figure 3 (c) shows the changes in the average speed of all vehicles vs. the traffic flow rate. The chart is plotted for various ratios of eco-driving assisted vehicles to evaluate the adverse effects of the proposed eco-driving on the traffic. The change in speed was about 1% until the traffic flow rate reached 720 vehicles/h. At the rate of 840 vehicles/h, however, the average speed began to decrease, and a decrease of 3 to 4% was observed when the ratio of vehicles assisted by the eco-driving system reached 80%.

These results confirm that the proposed eco-driving pattern, which is designed to minimize the delay time, has only a small impact on the surrounding traffic. However, at a greater traffic flow rate and a higher ratio of eco-driving assisted vehicles, this driving system may have adverse effects on the traffic.

4. Evaluation by Field Tests

Next, we built an in-vehicle information system as described in section 2, and conducted field tests to verify the effect of the eco-driving in an actual environment.

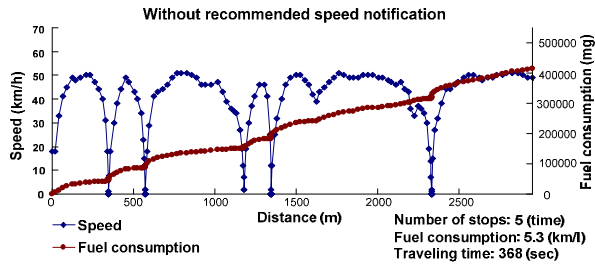
Table 1 summarizes the results of the field tests conducted in suburban and urban environments. While some improvement in fuel economy was observed in either environment, the eco-driving had a greater effect in the suburban environment.

Table 1 Average fuel cost in suburban and urban environments

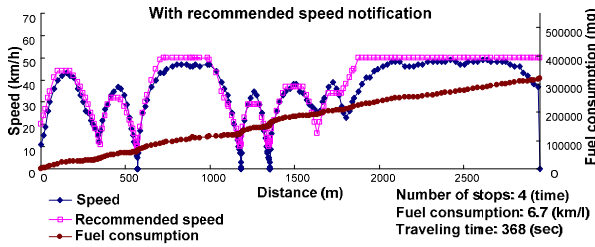
	With driving assistance	Without driving assistance	Increase
Suburban	7.45 (km)	8.25 (km/l)	11.5%
Urban	8.08 (km)	8.51 (km/l)	5.3%

Figure 4 shows an example pair of field test driving patterns: (a) normal driving without the eco-driving assistance and (b) with the assistance. The Recommended Speed in (b) shows a pattern from Recommended speed creation system, whereas Speed is that of vehicle driven along Recommended Speed. While the traveling times of (a) and (b) were equal, the eco-driving assistance suppressed the cruise speed and successfully reduced the number of major decelerations to 15 km/h or lower. In this example, together with additional effects of gradual acceleration from the stop position and early release of the accelerator pedal, the fuel consumption was reduced by about 25% from that without assistance.

Note that these field test data were obtained by participating in the experiments of the green wave driving system conducted by the Universal Traffic Management Systems (UTMS) Society of Japan.



(a) Without driving assistance



(b) With driving assistance

Fig. 4 Results of field testing

5. Challenges for the Future

The proposed eco-driving assistance with in-vehicle information system requires further evaluation under additional conditions.

LED Headlamp Driver

Authors: Yasuhiro Nukisato* and Naohiro Kishi**

1. Introduction

An over-current flowing into a light emitting diode (LED) may shorten its service life or even destroy it. Therefore, the LED headlamp driver for automobiles must suppress any over-current that may flow into the LED even if the supply voltage varies. Mitsubishi Electric has developed an LED driver that successfully suppresses the over-current by feed forward control and pulse width modulation (PWM) control with variable duty cycle. This paper describes how the over-current is prevented from flowing into the LED.

2. Overview of LED Headlamp Driver

2.1 Constant current control

The forward voltage of one LED chip is about 2 to 4 V depending on the temperature. LEDs are generally serially connected for low-beam operation (20 to 40 V for 10 chips), and thus the supply voltage needs to be boosted by a DC/DC converter to drive the LEDs.

LEDs have individual variations in luminance-current characteristics, and thus they are classified into various luminous flux ranks. In order for each LED in any rank to produce the same luminance, it needs to be individually controlled at a constant current corresponding to its luminous flux rank.

2.2 Telltale output

It is stipulated by law and thus mandatory that any input/output anomaly shall be detected and the operation shall be shut down, and that if LEDs are used for low-beam operation, the normal/abnormal condition shall be notified (Telltale) to the vehicle.

2.3 Luminance control

The luminance of the LED lamp needs to be controlled by changing the output current according to the lighting mode such as low-beam lights, position lights and daytime running lights (DRL).

3. Mitsubishi Electric's Element Technologies for LED Drivers

3.1 Constant current control corresponding to luminous flux rank

On each LED chip board, a resistor called a "rank resistor" is mounted corresponding to the LED's luminous flux rank. Before turning on the lamp, the rank

resistor is detected to perform constant current control corresponding to the luminous flux rank. Mitsubishi Electric's design is able to handle up to six different ranks.

3.2 Feed-forward control

The LED driver must be designed assuming that the supply voltage varies. Constant current control is generally performed by the feed-back system for the output current. However, with only feed-back control, an over-current may flow into the LED when the voltage changes abruptly.

Specifically, when the supply voltage abruptly rises from a low voltage (9 V) to a higher voltage (16 V), it is necessary to immediately shorten the ON time of the field effect transistor (FET) on the primary side of the DC/DC converter. However, in feed-back control, the ON time can be shortened only after an excessive current actually flows, and thus inevitably allowing an over-current to flow into the LED. Since an over-current may shorten the service life or damage the LED, some preventive measures need to be taken.

In response, we have employed feed-forward control to prevent the over-current from flowing into LEDs in the case of an abrupt change in the power supply voltage (voltage rise).

Figure 1 shows the waveforms of the feed-back control circuit when the supply voltage is changed from 9 V to 16 V. When the supply voltage is 9 V, a long FET ON time is observed. With this long ON time, the supply voltage is abruptly changed to 16 V, and thus an over-current starts flowing into the LED. This over-current cannot be avoided because the ON time is shortened after the over-current has started flowing into the LED.

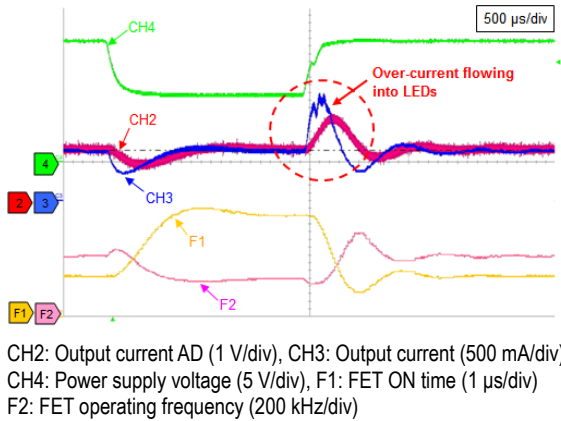
Figure 2 shows the waveforms of the circuit when feed-forward control is added. If an abrupt increase in the supply voltage is detected, the FET is controlled with the minimum ON time corresponding to the detected supply voltage, and thus the over-current into the LED can be suppressed.

3.3 Luminance control

The LED lamps are PWM controlled to produce various luminance levels by setting the duty cycle to 100% (DC operation) for the low beam, 80% for DRL, and 10% for position lighting mode. In any of these modes, the operating frequency remains the same at 400 Hz. While the duty cycle of the PWM is controlled by the DC/DC converter turning on and off, out of the

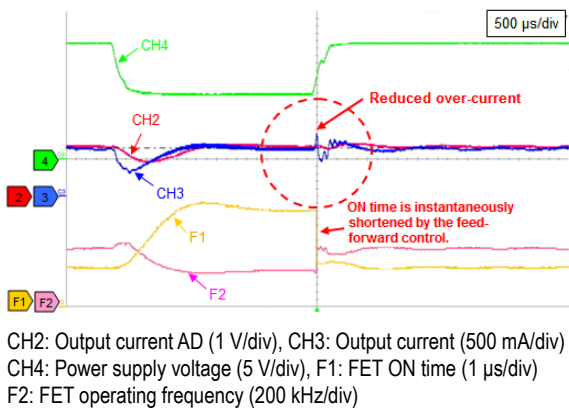
period of 2.5 milliseconds (400 Hz), the DC/DC converter is ON for 2 milliseconds in the DRL mode and 0.25 milliseconds in the position lighting mode.

The PWM control needs to be designed so that the output current reaches the rated level as quickly as possible to achieve a rectangular waveform. Therefore, as shown in Fig. 3, the FET on the primary side of the DC/DC converter is activated with the same ON time as the previous lighting cycle.



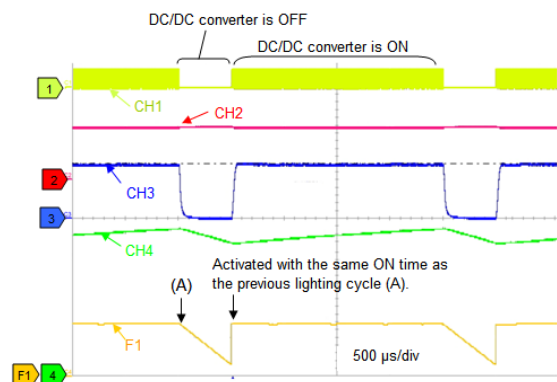
CH2: Output current AD (1 V/div), CH3: Output current (500 mA/div)
CH4: Power supply voltage (5 V/div), F1: FET ON time (1 μ s/div)
F2: FET operating frequency (200 kHz/div)

Fig. 1 Waveforms during a supply voltage change from 9 V to 16 V (Feed-back control)



CH2: Output current AD (1 V/div), CH3: Output current (500 mA/div)
CH4: Power supply voltage (5 V/div), F1: FET ON time (1 μ s/div)
F2: FET operating frequency (200 kHz/div)

Fig. 2 Waveforms during a supply voltage change from 9 V to 16 V (Feed-back/ Feed-forward control)

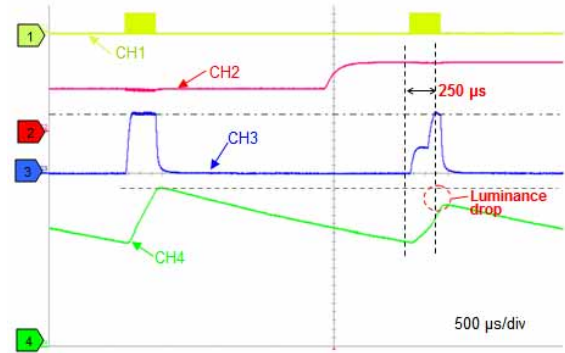


CH1: FET gate voltage (10 V/div), CH2: Power supply voltage (10 V/div)
CH3: Output current (500 mA/div), CH4: Luminance
F1: FET ON time (1 μ s/div)

Fig. 3 Waveforms during DRL operation (duty cycle: 80%)

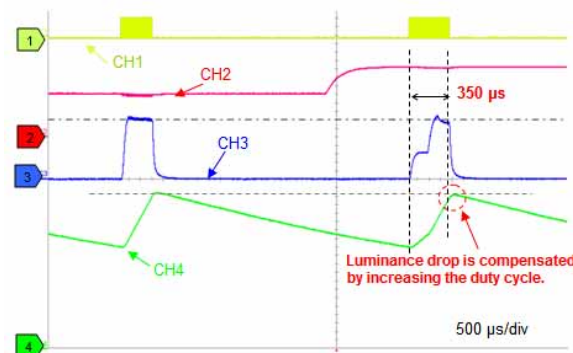
Note that the feed-back function is deactivated during a certain “mask period” after the startup of operation. This mask period prevents an overshoot of the output current, which may occur if the output current deviates far from the target level.

When the supply voltage changes during an OFF state of the DC/DC converter, to prevent an overshoot, the converter is turned on with the minimum ON time corresponding to the supply voltage at the turn-on timing, not the same ON time as the previous cycle. As a result, the LED remains dark until the feed-back control is activated after the mask period, and the “position” operation with a low PWM duty cycle may suffer from a significant drop in luminance (Fig. 4). This problem has successfully been overcome by increasing the duty cycle in case of such a supply voltage change (Fig. 5).



CH1: FET gate voltage (10 V/div), CH2: Power supply voltage (10 V/div)
CH3: Output current (500 mA/div), CH4: Luminance
F1: FET ON time (1 μ s/div)

Fig. 4 Change in supply voltage during “position” lighting (duty cycle: 10%)



CH1: FET gate voltage (10 V/div), CH2: Power supply voltage (10 V/div)
CH3: Output current (500 mA/div), CH4: Luminance
F1: FET ON time (1 μ s/div)

Fig. 5 Change in supply voltage during “position” lighting (duty cycle: 10%) after improvement

4. Conclusion

As the use of LED lamps for automotive applications increases, LED drivers require advanced functionality so that one driver is able to control a variety of lamps. To keep pace with the rapid spread of LED

applications, we will gain knowledge through this LED driver project, and promptly develop and release suitable products to contribute to society.

High Efficiency Isolated AC/DC Converter with Gradationally Controlled Voltage Inverter for On-board Charger

Authors: Takashi Kaneyama* and Ryota Kondo**

We have developed a new isolated AC/DC converter for electric vehicle on-board chargers. It consists of an AC/DC converter with Gradationally Controlled Voltage Inverter (GCVI AC/DC converter) and an isolated Zero-Voltage-Switching (ZVS) DC/DC converter, each of which is optimally controlled to convert in a highly efficient means. As a result, the new on-board charger has achieved a power conversion efficiency of over 94%.

1. Introduction

Generally, an Electric Vehicle (EV) is equipped with an on-board charger to charge its large-capacity battery from an Alternating Current (AC) power outlet. The rate of consumption of AC electric energy, which is defined as the ratio of the driving distance to the electric energy charged from the grid power, is one of a key factor for an EV; to improve it, the on-board charger is required higher efficiency of conversion. This paper describes technologies for improving the efficiency of the isolated AC/DC converter and the application examples to the on-board charger.

Figure 1 shows the converter configuration and technologies of the new on-board charger. The AC/DC converter circuit employs a Gradationally Controlled Voltage Inverter (GCVI) technology, which is based on our original multi-level inverter technology that can reduce both power loss and electromagnetic noise. While the GCVI has already been applied to the voltage sag compensator⁽¹⁾ and other inverter devices, we newly applied this technology to the converter circuit⁽²⁾ and have developed a new on-board charger. The isolated DC/DC converter employs the Zero-Voltage-Switching (ZVS)⁽³⁾, which is soft switching method with low switching loss. In addition, we have

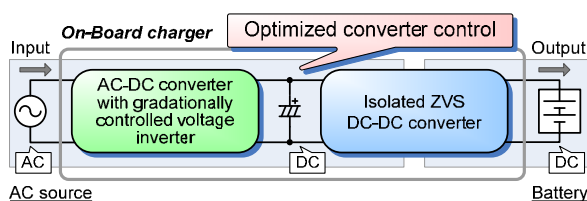


Fig. 1 Converter configuration and applied technologies in the on-board charger

developed an optimized converter control technology⁽⁴⁾ to achieve high efficiency of conversion in a wide range of input/output voltages.

2. Employed Technologies

2.1 GCVI AC/DC converter

2.1.1 Gradationally controlled voltage inverter (GCVI)

Figure 2 shows a schematic circuit diagram of the GCVI AC/DC converter. This circuit is configured with a general AC/DC step-up converter being connected to a GCVI circuit, which consists of series-connected inverter units. By controlling these inverter units so that a capacitor C_2 has twice as much voltage as C_1 , e.g., $2V_0$ and V_0 , the output voltage of GCVI V_{inv} can have seven different values from $-3V_0$ to $+3V_0$ according to the combination of switching pattern. The GCVI can also select charge/discharge of C_1 from switching pattern when $V_{inv} = +V_0$ or $-V_0$, then it can control the C_1 to C_2 voltage ratio to be two.

2.1.2 Operation principle of AC/DC converter

For the Power Factor Correction (PFC), the GCVI AC/DC converter controls the AC input current to be a sinusoidal wave in phase with the AC input voltage V_{ac} . By controlling the GCVI so that the amplitude of V_{inv} in the Pulse Width Modulation (PWM) period equals V_0 , an input current ripple due to switching can be reduced and controllability of the input current is improved, which also enables the size of the PFC reactor to be reduced and the switching frequency to be lowered. In

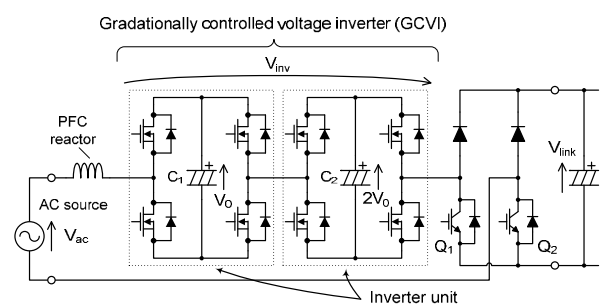


Fig. 2 Schematic diagram of the GCVI AC/DC converter

addition, since the voltage required for the current control is distributed to each inverter unit, the switching voltage for the current control is lower than that of a general AC/DC step-up converter. As a result, the switching loss can be reduced, and the electromagnetic noise can be also suppressed.

Figure 3 shows the gate waveform of the switching devices Q_1 and Q_2 with the AC input voltage. During the ON period of Q_1 and Q_2 , the GCVI controls AC current by outputting against the AC voltage V_{ac} , and C_1 , C_2 are charged. While the OFF period of Q_1 and Q_2 , the GCVI controls AC current by adding to V_{ac} , and C_1 , C_2 are discharged. Therefore, by controlling the ON period (phase θ_1) of Q_1 and Q_2 , the voltages of C_1 and C_2 can be controlled. The switching voltages of Q_1 , Q_2 is equal to the output voltage of the AC/DC converter V_{link} , but the switching frequency is just four times an AC period, so the switching losses of Q_1 , Q_2 are very low.

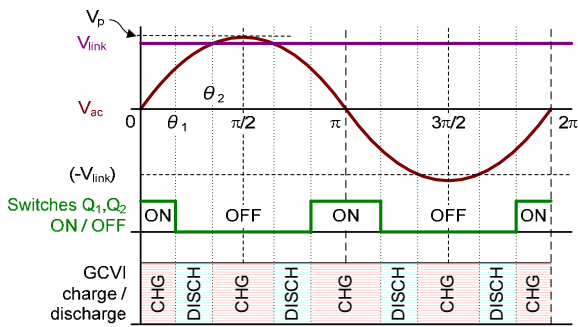


Fig. 3 Gate waveform of switching devices Q_1 , Q_2 with AC input voltage

As shown in Fig. 3, the GCVI AC/DC converter can control V_{link} at a lower voltage than the AC peak voltage, V_p . As a result, the GCVI AC/DC converter allows the use of an output device with a lower withstand voltage compared to the conventional converter, and the loss can also be reduced. While the GCVI AC/DC converter works stably, the charge and discharge energy of C_1 , C_2 during one period of the AC input voltage are equal, and then the relationship between V_{link} and phase θ_1 is given by the following equation:

$$V_{link} = V_p \cdot \pi / 4 \cos \theta_1 \quad (1)$$

The lowest voltage is given at phase $\theta_1 = 0$, which gives " $V_{link} = V_p \cdot \pi / 4$."

2.2 Isolated ZVS DC/DC converter

Figure 4 shows the schematic diagram of the isolated ZVS DC/DC converter. It is based on a full-bridge isolated DC/DC converter circuit, resonant capacitors are connected to switching devices for ZVS in parallel, and a resonant reactor is connected to the high frequency transformer in series. While the period of free-wheeling, the primary current flows through the loop

between the switching devices and the transformer, and power is not transferred to secondary side, so the conduction losses increase. Thus, shortening the free-wheeling period causes higher efficiency in the ZVS DC/DC converter.

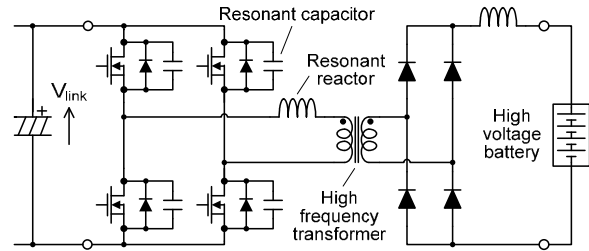


Fig. 4 Schematic diagram of the isolated ZVS DC/DC converter

2.3 Optimized converter control

The optimized converter control is our original technology, which controls V_{link} as low as possible to reduce the power loss of the isolated ZVS DC/DC converter.

With this technology, the freewheeling period of the DC/DC converter is shortened and the conduction loss can be reduced. In addition, because of its low V_{link} , the resonance energy for the ZVS operation is reduced. Therefore, it expands the range of ZVS operation and enables the switching energy to be reduced. Furthermore, the GCVI AC/DC converter allows step-down operation and thus further expands the range of ZVS operation compared to the conventional AC/DC converter.

3. Performance

Figure 5 shows the external appearance and specifications of the newly developed on-board charger.

Figure 6 shows the input/output waveforms of this on-board charger operated with a supply voltage of AC 200 V and battery voltage of DC 370 V. The input current is controlled well with a power factor of over 99%. In addition, as shown in Fig. 7, when operated at the maximum power with the battery voltage ranging from DC 200 to 370 V, the power conversion efficiency is over 92% and the maximum efficiency exceeds 94%.



Input voltage	85 - 260 [Vrms] (AC)
Output voltage	200 - 370 [V] (DC)
Maximum input current	15 [Arms] (AC)
Maximum output current	12 [A] (DC)
Maximum output power	3.5 [kW]
Dimensions	W235 x D275 x H143 [mm]
Weight	11.5 [kg]

*Including 12V Step-down converter

Fig. 5 On-board charger with GCVI

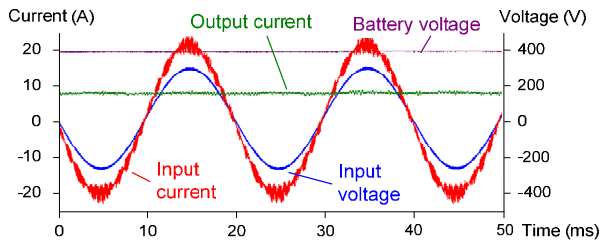


Fig. 6 Waveform of input and output current (200 VAC input, 370 VDC output)

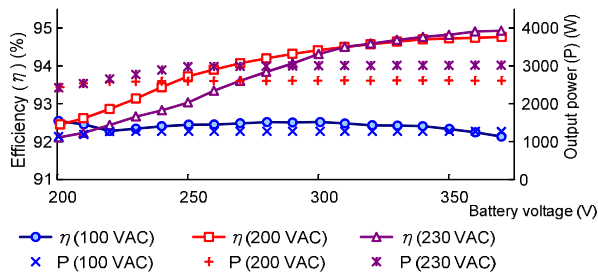


Fig. 7 Characteristics of battery voltage vs. power conversion efficiency

4. Conclusion

We have developed a high-efficiency isolated AC/DC converter for on-board chargers, which employs our original Gradationally Controlled Voltage Inverter (GCVI) technology and optimized converter control technology. The newly developed on-board charger provides a high power conversion efficiency of over 92% over a wide voltage range and the maximum efficiency exceeds 94%.

The newly developed technologies are also applicable to other on-board chargers with different power ratings, as well as to other products consisting of an AC/DC converter and an isolated DC/DC converter.

References

- (1) M. Yamada et al.: A New Voltage Sag Compensator with a Gradationally Controlled Voltage Inverter, Proc. of Power Electronics and Applications, 2005 European Conference, pp. 1-7.
- (2) S. Murakami et al.: Development of High Efficiency Gradationally Controlled Voltage Inverter with Step Up and Down Function, Proc. of JIASC2010, pp. I_421-I_424. (in Japanese)
- (3) G.J. Torvetjonn et al.: A DC/DC Converter Topology with Phase Shift Control and Lossless Snubbers for Use in a 200A Battery Charger Working on 400V Mains, Proc. of Telecommunications Energy Conference, 1995. INTELEC '95, 17th International, pp. 489-495.
- (4) T. Kaneyama et al.: High Efficiency Isolated AC/DC Converter with Gradationally Controlled Voltage Inverter for On-Board Charger, SAE Int. J. Alt. Power. 2(2): 389-393, 2013.

Next-generation Motor Controller Unit for Electric Power Steering

Authors: *Yoshihito Asao** and *Yoshihiko Kimpara***

The motor controller unit (MCU) for electric power steering (EPS) needs to be smaller and lighter to provide a superior steering feel as well as to improve fuel consumption and mountability. To meet these needs, a next-generation MCU has been developed and put into mass production by fully integrating an optimized internal structure, electromagnetic design and high-output control (Fig. 1).



Fig. 1 Next-generation motor controller unit

1. Features of Next-generation MCU - Motor

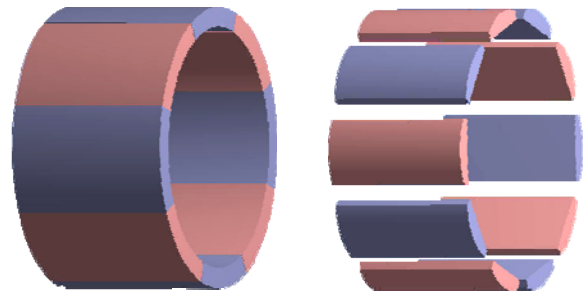
To achieve a small and light body as well as a superior steering feel, the next-generation MCU motor uses a "Poki-Poki" core, 10-pole-12-slot system, delta-connection and segment magnets.

The *Poki-Poki* core is Mitsubishi Electric's original technology, where wires are first wound on a linearly extended core which is then formed into a circular shape. For the next-generation MCU motor, the conventional *Poki-Poki* core design has been further improved to compensate manufacturing variations of the cores and rotors and reduce cogging torque which adversely affects the steering feel.

The combination of the numbers of magnet poles and stator slots was reviewed and the conventional 8-pole/12-slot design has been modified to a 10-pole/12-slot combination. This 10-pole-12-slot system provides a high winding factor for the fundamental harmonic, which means high efficiency of magnetic flux utilization and enables the magnet volume per unit generated torque to be reduced. On the contrary, the new system provides low winding factors for the higher

harmonics (5th and 7th), which reduce the torque ripple and thus improve the steering feel.

In contrast to the ring-type magnet of the current-generation product, the next-generation product employs a segment magnet (Fig. 2). In combination with the optimized electromagnetic design, the magnet volume has been reduced by about 40% from the ring-type magnet. The torque ripple and cogging torque have also been reduced by optimizing the magnet shape.



Current generation: Ring shaped magnet Next generation: Segment magnet

Fig. 2 Comparison of magnet shapes

2. Features of Next-generation MCU - Controller

In the next-generation MCU, a motor and a controller are integrated and arranged on the same axis to reduce the size, weight, and cost.

Figure 3 shows the internal structure of the next-generation MCU. On the heat sink, an inverter circuit is mounted to drive the motor, consisting of three compact power modules, each of which corresponds to each of three phases, and a relay module for isolating the MCU from the external power supply. These four modules in total are concentrically arranged and evenly spaced. Between these modules, large capacitors and choke coils are also concentrically arranged to achieve electromagnetic compatibility (EMC). Connection terminals for these large components are put together in the insert-molded single resin frame.

3. Features of Next-generation MCU - Control System

To achieve a superior steering feel for the next-generation MCU, we have developed a motor control system for better stabilization with an improved

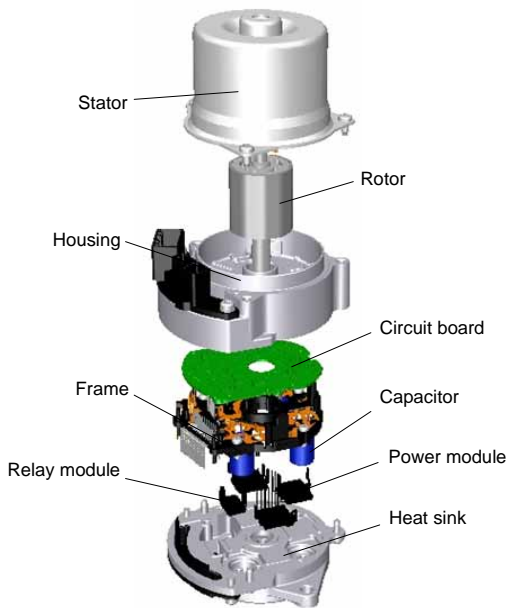


Fig. 3 Internal structure of next-generation MCU

damping performance and better adaptability to high rotation speed of the steering wheel.

When driving on a stone-paved or similar road surface, uncomfortable vibration is sometimes propagated to the steering wheel. The new control system successfully reduces such vibration thanks to a software damper that controls the motor based on the steering torque and the rotation speed of the motor. This system provides a superior steering feel by ignoring those vibrations in the frequency band associated with the driver's steering actions, while effectively damping vibrations in higher frequency bands.

When the rotor rotates, the magnetic flux from the rotor changes, and then an electromotive force is generated in the stator coil by electromagnetic induction. This electromotive force is generated in such a direction that an associated electric current opposes a change in the rotor's magnetic flux. This force is called counter-electromotive force, and the faster the steering wheel is rotated, the greater the counter-electromotive force is. When the next-generation MCU detects an increase in the rotation speed of the steering wheel, the control system reduces the counter-electromotive force by providing the motor with an electric current in the direction to oppose the rotor's magnetic flux.

4. Features of Next-generation MCU - Packaging

Compared to the current-generation MCU with an equivalent output power, the next-generation MCU has been made 50% smaller in volume and 30% lighter, by arranging the controller and motor on the same axis, downsizing and optimally arranging the built-in parts, and rationalizing the connecting components. The new

MCU significantly improves the mountability on the vehicle and reduces the fuel cost. Table 1 summarizes the key specifications of the next-generation MCU, and Fig. 4 shows a physical comparison of the current- and next-generation MCUs both having the same output power.

Table 1 Specifications of next-generation MCU

Item	Specification
Diameter (Controller)	93 mm
Diameter (Motor)	80 mm
Length	100 mm - 140 mm
Weight	1.8kg - 3.3kg
Rated torque	2.2 Nm - 6.8 Nm

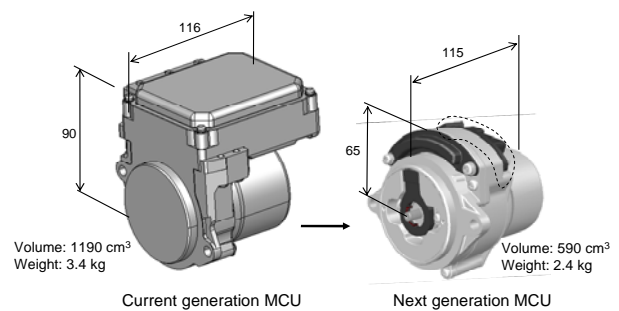


Fig. 4 Physical comparison of MCUs

Because of its large size, the current-generation MCU needs to be custom designed to suit the customer's request for the vehicle layout and connector specifications. For the next-generation MCU, the connector port has been modularized (surrounded by the dashed line in Fig. 4) and only the connector can be modified as required by the customer.

We will continue to help reduce automobile fuel consumption by offering next-generation MCUs to automobile and steering manufacturers.

Study of Fuel Adhesion Behavior during Spray-wall Impingement in PFI Engine

Authors: Takashi Yonezawa* and Kazuhiko Kawajiri*

A new method has been proposed and experimentally verified for evaluating the amount of adhered fuel when the fuel spray is injected from an automotive injector and impinges on the wall surface. It has been confirmed that the proposed method can describe the relationship between the incident angle of the spray droplet and the amount of adhered fuel on the wall, which is not possible by the conventional simulation.

1. Introduction

In recent years, with growing awareness of energy saving and global environmental conservation, it is increasingly important to improve automobile fuel economy and reduce exhaust gas emissions. In the port fuel injection (PFI) engine, a fuel spray is injected into the intake port and a part of that spray impinges on the wall surface, where complex phenomena are taking place such as adhesion and flow with evaporation. The behavior of the fuel adhered on the wall significantly affects the fuel economy and exhaust gas characteristics, and thus it is important to understand the adhesion behavior.

This paper presents our new numerical simulation method and its verification for evaluating the adhesion behavior of the fuel spray when it is injected from an automotive injector and impinges on the wall surface. The verification was performed by fundamental experiments involving injecting fuel sprays onto a flat plate⁽¹⁾.

2. Proposed Method for Evaluating Amount of Fuel Adhered during Spray-Wall Impingement

When fuel sprays impinge on the wall surface, various adhesion behaviors take place depending on the velocity and diameter of the droplets and other impingement conditions. The types of behavior range from all adhered to all reflected, including partially adhered and re-dispersed otherwise (referred to as “splashing”). In the conventional simulations of spray-wall impingement, the ratio between the adhered and re-dispersed fuel of splashing is assumed to be constant regardless of the impingement conditions⁽²⁾, or the fraction of re-dispersed fuel is assumed to increase with the increase in impact velocity of the droplet normal to the wall surface⁽³⁾. In the case of splashing, the

mass and kinetic energy of the impinging droplet are first absorbed into the liquid film on the wall surface. Subsequently, a part of the absorbed energy is consumed and some droplets are re-dispersed (Fig. 1). Therefore, the ratio between the adhered and re-dispersed fuel is thought to depend on the incident angle and energy of the droplet. According to the conventional simulations, however, the amount of re-dispersion droplets remains unchanged regardless of the incident angle of the spray droplets, or oblique impingement reduces the normal component of the droplet velocity and hence the amount of re-dispersed fuel. As such, if the incident angle of the impinging droplet varies, it was impossible to accurately evaluate the amount of fuel adhered on the wall surface. This paper proposes a method to evaluate the amount of adhesion during splashing at different incident angles of the fuel spray.

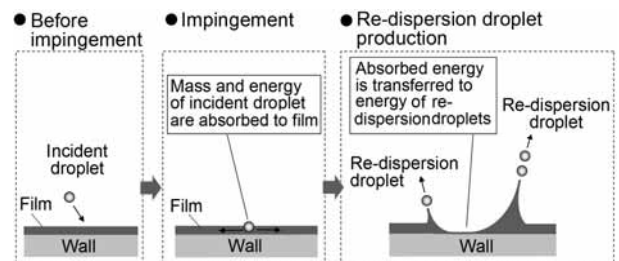


Fig. 1 Outline of splash behavior

The wall adhesion behavior in the splashing process is thought to be affected not only by the normal component of the droplet velocity but also by the tangential component. Therefore, the proposed method takes into consideration the droplet velocity tangential to the wall surface, which was previously not considered. The re-dispersed fraction of impinging droplets is expressed by Eq. (1), in terms of the normal Weber number, We_{in-n} , based on the incident droplet velocity normal to the wall, V_{in-n} , and the tangential Weber number, We_{in-t} , based on the tangential velocity, V_{in-t} (Fig. 2).

$$\frac{M_{out}}{M_{in}} = C \times \{ C_n \times We_{in-n} + (1 - C_n) \times We_{in-t} \} \quad (1)$$

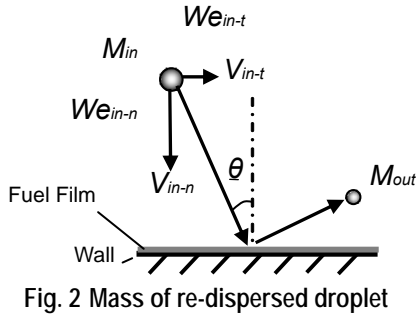


Fig. 2 Mass of re-dispersed droplet

where, $We_{in-n} = \rho d V_{in-n}^2 / \sigma$, and $We_{in-t} = \rho d V_{in-t}^2 / \sigma$; ρ : density, d : droplet diameter, V : droplet velocity, and σ : surface tension. C and C_n are the coefficients and C_n ranges from 0 to 1.

3. Verification by Spray - Plate Impingement and Adhesion Experiment

3.1 Method of experiment

To verify the proposed method for evaluating the adhesion characteristics of the splash behavior, the fuel sprays were injected onto a wall surface and the amount of adhered fuel was measured. Figure 3 illustrates the outline of the experimental apparatus, where a dual spray injector with 10 holes is installed and a low-volatility dry solvent is used as the fuel (Table 1).

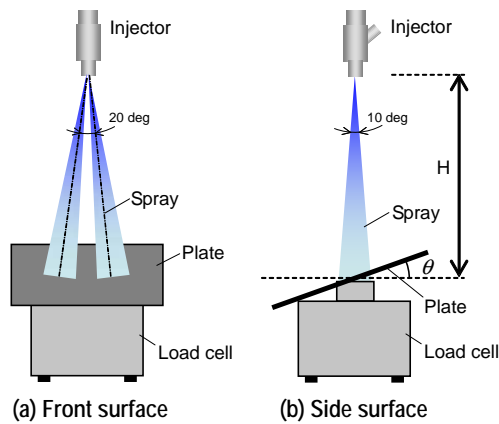


Fig. 3 Outline of experimental apparatus

Table 1 Experimental conditions

Ambient pressure	0.1 MPa
Injected pressure	0.37 MPa
Fuel	Drysolvent
Ambient & Wall temperature T	296 K
Plate surface roughness R	Ra 10 μm
Injector-wall distance H	50, 75, 100 mm
Wall inclination angle θ	0, 45 deg

3.2 Results of experiment

Figure 4 shows the measurement result when varying the injector-wall distance, H , and the wall inclination angle, θ . The vertical axis shows the fraction of adhered fuel (= mass of adhered fuel/mass of all in-

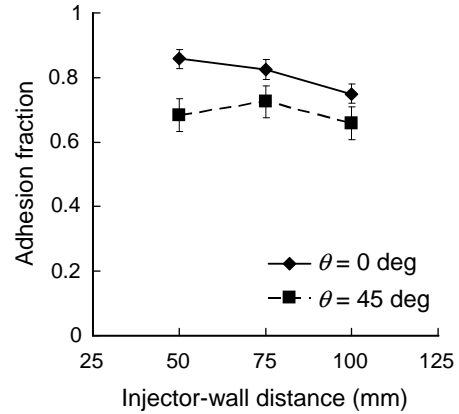


Fig. 4 Variation of adhesion mass fraction at different spray inclination angles

jected fuel). When H is changed, the behavior at $\theta = 0$ deg differs from that at $\theta = 45$ deg. When $\theta = 0$ deg, as H increases the amount of adhesion monotonously decreases. With the increase in H , more and more spray droplets float in the air and less fuel reaches the wall surface, and thus the amount of adhesion decreases. In contrast, when $\theta = 45$ deg, the amount of adhesion at $H = 75$ mm is greater than that at $H = 50$ mm, showing a trend opposite to the case when $\theta = 0$ deg. It is thought that the impact velocity of spray droplets impinging on the wall at $H = 50$ mm is greater than that at $H = 75$ mm, and the amount of re-dispersed droplets increases in excess of the amount of adhered droplets, resulting in the decrease of adhered fuel.

3.3 Numerical simulation method

The wall impingement behavior of the spray droplets was simulated using the spray impingement model of Bai et al.⁽²⁾, and Eq. (1) was used to calculate the mass fraction of the re-dispersed droplets. For comparison, the conventional calculation was also performed based on the impingement velocity normal to the wall surface⁽³⁾. The coefficients C and C_n in Eq. (1) were determined as $C = 0.0015$ and $C_n = 0.13$ so that the proposed method and the conventional evaluation agreed in terms of the mass fraction of the re-dispersed droplets when the spray droplets impinge normal to the wall surface. The spray droplet behaviors were calculated in a Lagrangian manner using the discrete droplet model (DDM). Breakup of the droplet was simulated by the bag and stripping breakup model of Reitz et al., but droplet recombination was not considered. In this simulation, the diameter, velocity and direction of the spray droplets were predetermined so that the simulation results of the spray shape formed by the injector, spray distribution, spray penetration, and Sauter mean diameter matched those of the experiment.

3.4 Verification of numerical simulation

Figure 5 shows the comparison of the experimental and calculation results. According to the conventional evaluation method, when the wall inclination angle $\theta = 0$ deg, the calculation and experimental results agree with each other, but when $\theta = 45$ deg, they do not agree at the injector-wall distance of $H = 75$ mm or less. In contrast, according to the proposed Equation (1), which takes into consideration that the amount of re-dispersion varies depending on the incident angle of the impinging droplet, the calculation results are in good agreement with the experimental results of the fuel adhesion during the spray-wall impingement. Note that the splash behavior rarely occurs at $H = 100$ mm or greater, and thus no difference is observed between the two evaluation methods.

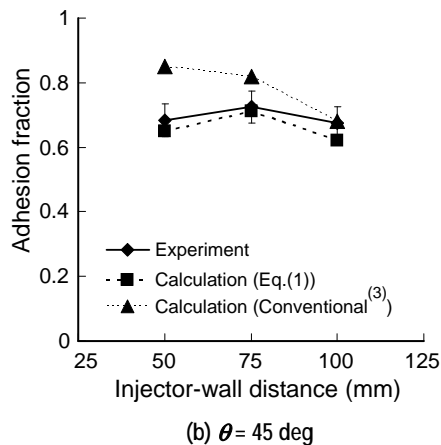
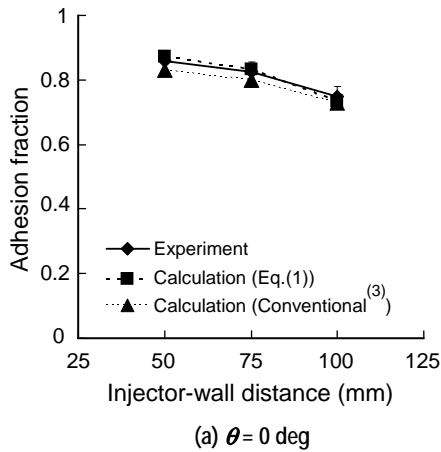


Fig. 5 Comparison of adhesion mass fraction

4. Conclusion

In this paper, a new method has been proposed for evaluating the amount of adhered fuel when fuel spray is injected from an automotive injector and impinges on the wall surface. The new method was verified by a fundamental experiment of injecting fuel sprays onto a flat plate. As a result, it was verified that the proposed method is able to describe the relationship between the

incident angle of the spray droplet and the amount of fuel adhered on the wall, which is not possible by the conventional simulation.

By fully utilizing this numerical evaluation method, we will contribute to the development of next-generation engines and components that will improve fuel economy and lower exhaust gas emissions.

References

- (1) T. Yonezawa and K. Kawajiri: Study of Adhesion Fuel Behavior Formed by Spray-Wall Impingement in PFI Engine, SAE-paper 2010-01-0782 (2010)
- (2) C. Bai and A.D. Gosman: Development of Methodology for Spray Impingement Simulation, SAE950283 (1995)
- (3) Z. Han, Z. Zu and N. Trigui: Spray/wall Interaction Models for Multidimensional Engines Simulation, Int. J. Eng Research, Vol. 1, No. 1 (2000)

Telematics-compatible Information Security Technology

Authors: Nobuhiro Kobayashi* and Manabu Misawa*

For telematics-compatible in-vehicle information systems, security related requirements and issues were reviewed, and a new system has been proposed to prevent an increase in the processing load on in-vehicle equipment, to ensure long-term security strength, and to keep the security system functioning in case of disrupted communications and other troubles.

1. Telematics and Security

Recently, in-vehicle information systems have become more sophisticated, and attention is now focused on telematics, where services are provided by communicating and collaborating with external IT systems. Meanwhile, threats of remote intrusions and attacks on the in-vehicle system through the communications channel have been reported, and therefore new measures are required for information security⁽¹⁾.

An in-vehicle information system consists of vari-

ous electronic control units (ECUs), sensors, actuators, information devices, etc. connected to the main in-vehicle network. Their functions are divided into three categories: (1) basic control functions, (2) extended functions, and (3) general functions (Fig. 1).

Functions (1) are the basic indispensable functions for driving, turning, and stopping, which are closely related to the automobile's safety. Functions (2) are those for assisting the driver and improving the driving comfort; and telematics belong to this category. Functions (3) are provided by the mobile car navigation system and other devices brought in by the driver. The use of telematics is unlikely to allow direct attacks on the functions (1). However, indirect attacks via some function (2) may be attempted, and thus, security measures for category (2) are important when implementing a telematics system.

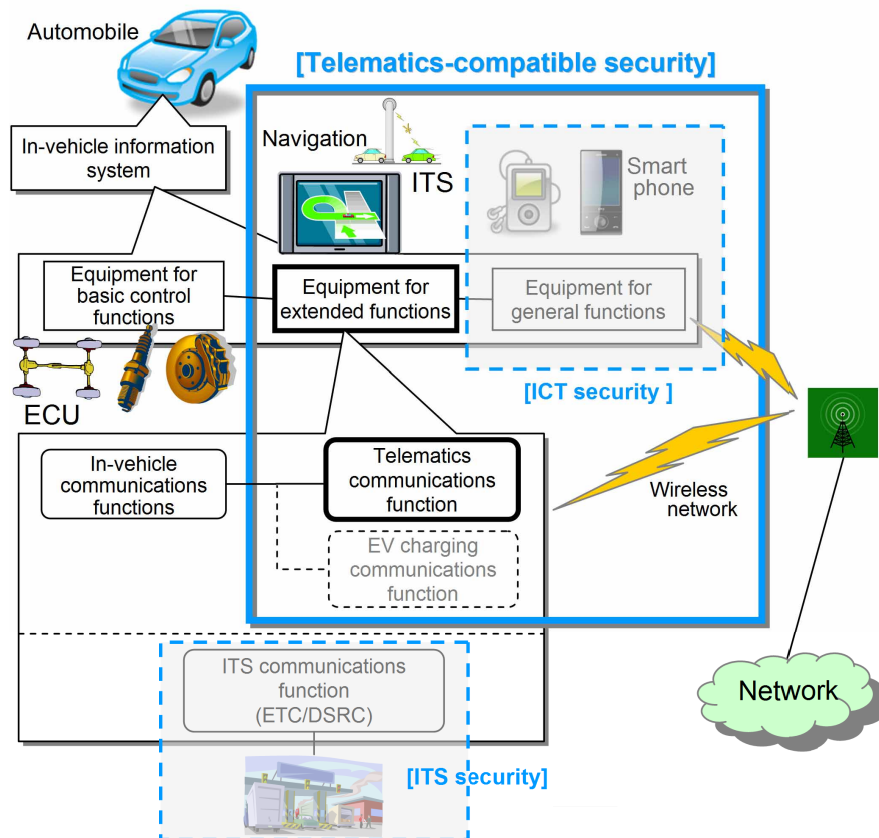


Fig. 1 Scope of telematics-compatible security

2. Requirements Analysis for In-vehicle Information System

The public key infrastructure (PKI) is widely used as an authentication scheme for Internet security⁽²⁾, and certificates issued by a certification authority (CA) are used for server authentication. In order for telematics to develop rapidly and effectively integrate with various services, it makes sense to use the same authentication scheme as on the Internet.

The characteristics of the in-vehicle information system are as follows. Statistically, the average service life of automobiles is 12 years or more. Allowing for the development period, the security must be sufficiently strong for the next 20 years ahead. In addition, when driving through an urban tunnel or grade-separated crossing, or on a mountainous route, communications with external networks may be disrupted. Furthermore, a system failure at the communications service provider may interrupt communications.

When considering the purpose of automobiles, the top priority is the safety of the human body and life. Therefore, the order of priority of the three elements of critical infrastructure security is the same as that of the control system: availability, integrity, and confidentiality. The requirements are summarized as follows:

- Requirement 1. The authentication scheme must be widely used on the Internet.
- Requirement 2. Security must be sufficiently strong for long-term operation.
- Requirement 3. The top priority is safety and security, with an emphasis on availability.

3. Issues of Security

Issue 1) In order to implement authentication by means of certificates, the authentication functions must include a process for verifying the certificate. In particular, verification of revocation requires obtaining a certificate revocation list (CRL) from each CA that has issued the certificates, and verifying the validity of the CRL itself. Each CRL can be enormous in size because it contains all certificates revoked before their expiration. In addition, the CRL is issued by each CA and thus downloading all CRLs can generate heavy communications traffic. Therefore, it is impractical to verify the revocation of an authentication certificate in the in-vehicle information system.

Issue 2) In order to ensure security for long-term use of automobiles, the cryptographic algorithm and key length must be adequate. The security of cryptographic algorithms degrades over time due to improvements in decryption technology and enhanced computer processing capacity. In order to ensure the security strength until the year 2030, the key length of the RSA cryptographic algorithm needs to be at least 2,048 bits, which increases the processing time for certificate verification, as well as the required memory size. As a result, the limited resources of the in-vehicle information system will be squeezed even tighter.

4. Proposed System

Based on the requirements and issues described above, we propose a new method for a secure in-vehicle system based on certificate authentication, where collaboration takes place between the automobile and a secure server, which is one of the telematics services (Fig. 2).

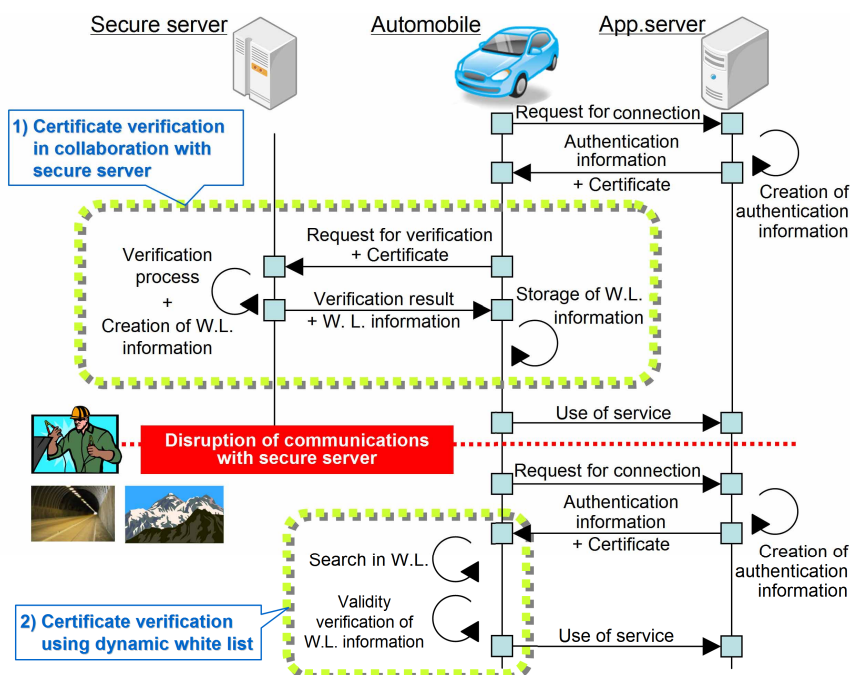


Fig. 2 Authentication process of proposed system

(1) Certificate Verification in Collaboration with Secure Server

First, as a countermeasure to Issue 1), the certificate verification including revocation check is executed by the secure server. The secure server has sufficient computer resources and a high-speed, highly reliable communication infrastructure, and thus can perform the certificate verification including revocation check with powerful processing performance and reliability. This method, by using powerful processing capability on the server side, also provides a solution to Issue 2), degradation of processing performance associated with the increase of key length, for ensuring long-term security.

(2) Certificate Verification Using Dynamic White List

The telematics-compatible security function must still work in case of a disruption of communications. In response, a white list (W.L.) is used to enable the in-vehicle system to perform the certificate verification process by itself. The W.L. contains the information of valid certificates, which have been verified by the secure server (W.L. information). In addition to verifying the certificates, the secure server generates W.L. information so that no additional processing by the in-vehicle system is required. The W.L. stored on the vehicle is dynamically updated to the latest version by the W.L. information. As a result, if collaboration with the secure server is interrupted, a matching test between the W.L. and the certificate provides simplified verification capability on board. Therefore, even if communications are disrupted, the security function continues to work because the authentication process is based on the security pre-checked certificate. There is also an advantage in case the system is configured without a secure server. That is, the processing load on the in-vehicle system can be reduced by pre-installing permanently reliable W.L. such as the W.L. information of automobile manufacturers.

(3) Resources Saving by Using Hash Values

The cost of in-vehicle microcomputers depends not only on their processing performance but also on the amount of installed memory. If the contents of certificates are stored as they are for the W.L. information, the required memory area increases in proportion to the number of certificates, which could have an impact on the limited in-vehicle resources. Consequently, a hash value of the certificate is provided as the W.L. information, which saves resources as follows (Table 1).

Table 1 Parameters for estimation

Trust model of PKI	CA 2 layers
Public key cryptographic algorithm	RSA, Key length: 2,048 bits
Hashing algorithm to generate W.L. information	SHA 256

According to the estimation, the data directly related to the cryptography and signature is reduced to 19.7% from 1,536 octets to 302 octets, so the proposed system can be used for in-vehicle equipment with very limited resources.

This system is also applicable to a wide variety of built-in security sensitive devices, as well as to various certificate-based services and protocols.

References

- (1) S. Checkoway, D. McCoy, B. Kantor, D. Anderson, H. Shacham, S. Savage, K. Koscher, A. Czeskis, F. Roesner, and T. Kohno: Comprehensive Experimental Analyses of Automotive Attack Surfaces, Proceedings of the 20th USENIX Conference on Security, pp. 77-92, USENIX Association, 2011
- (2) The Internet Engineering Task Force: RFC5280 Internet X.509 Public Key Infrastructure Certificate and Certificate Revocation List (CRL) Profile, May 2008, <http://tools.ietf.org/html/rfc5280>

